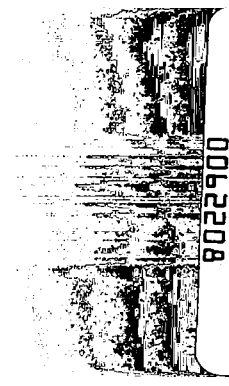

NASA Contractor Report 3532

Theoretical Design Study of the MSFC Wind-Wheel Turbine

Walter Frost and Philip A. Kessel

CONTRACT NAS8-34387
MARCH 1982

NASA

NASA Contractor Report 3532

Theoretical Design Study of the MSFC Wind-Wheel Turbine

Walter Frost and Philip A. Kessel
FWG Associates, Inc.
Tullahoma, Tennessee

Prepared for
Marshall Space Flight Center
under Contract NAS8-34387

National Aeronautics
and Space Administration

**Scientific and Technical
Information Branch**

1982

ACKNOWLEDGMENT

The authors are grateful for the funding provided by NASA, Marshall Space Flight Center, in support of this study. They are also grateful for the technical guidance and inputs provided by Mr. John W. Kaufman, Atmospheric Sciences Division, Space Sciences Laboratory. Finally, they wish to acknowledge the cooperation and assistance given them by Mr. Ismail Akbay, New Technology Officer.

TABLE OF CONTENTS

LIST OF ILLUSTRATIONS

1.0 SYSTEM DESCRIPTION

A mathematical evaluation of an innovative wind-wheel turbine (WWT) to evaluate overall design features was carried out. The conceptual basis of the WWT* studied was conceived by Mr. John W. Kaufman, NASA, Marshall Space Flight Center, in April, 1976.

The WWT apparatus is illustrated in Figures 1 through 4. The main parts of the WWT are: (1) a bladed wheel, (2) a main housing, (3) two forward ducts (front concentrators), (4) one duct on each side of the main housing (side concentrators), (5) an elevated base to support the functional parts of the WWT, and (6) an electrical/mechanical subsystem to be determined. The apparatus directs air (wind) onto the blades of the unexposed portion of a rotatable wheel through the multiple ducts and by direct impingement of wind onto the exposed top half of the bladed wheel, Figure 5. The forced rotation of the wheel can then be converted to power through appropriate subsystems.

Air entering the forward scoop is divided and accelerated by two venturi tubes which funnel it upward to the blades. Air flowing across the top of these scoops impinges on the exposed blades at the top of the wheel. Air flowing past the sides is scooped into the venturi tube which turns it 180° and expels it against the blades at the bottom of the wheel. As the wheel turns, "used" air leaves an exhaust vent at the bottom. The WWT is mounted on a pivot so that it can "weather vane" to face the wind.

Although wind-driven machines bearing some superficial resemblance to a water wheel have been developed in the past, the proposed concept has a certain distinguishing feature. The effectiveness of the machine will be improved by utilizing a number of fixed ducts to direct the wind from different directions onto the wheel. Ducts will be constructed with diminishing cross sections to accelerate the wind consistent with thermodynamic constraints to increase power output.

---

*United States Patent No. 4,191,505.

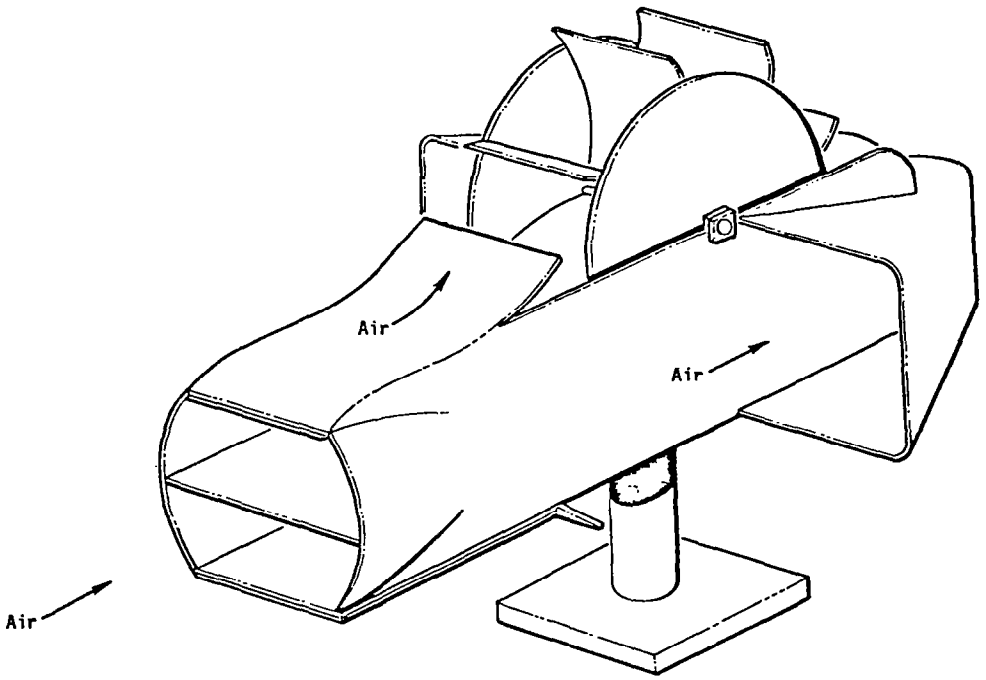

Figure 1 WWT preliminary design.

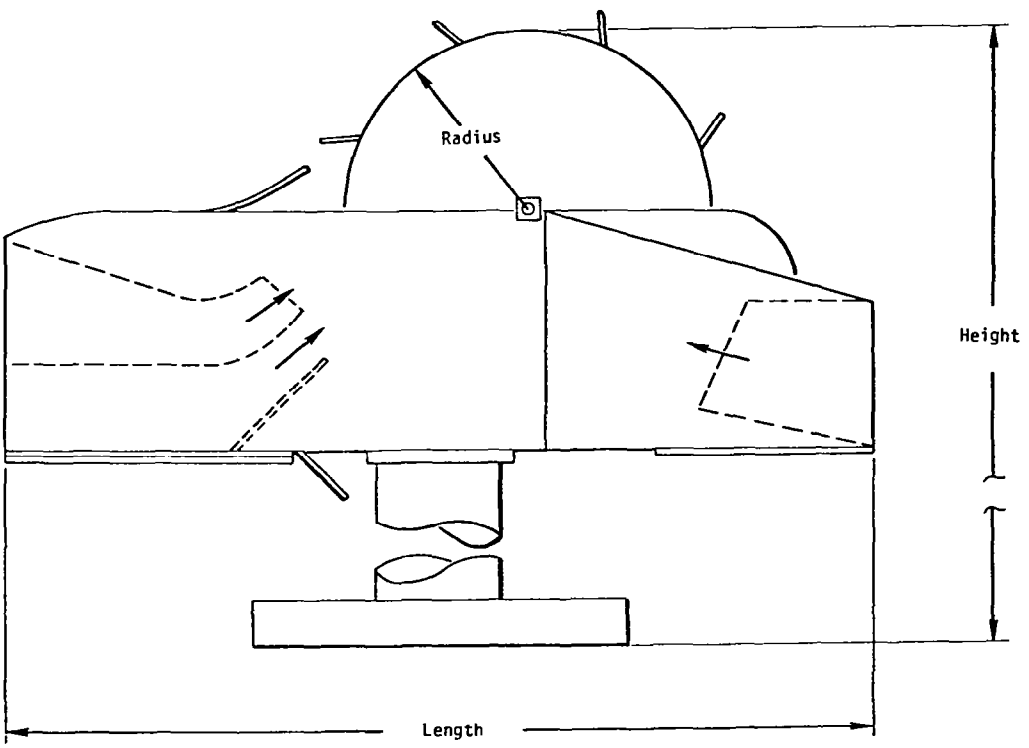

Figure 2 Side view of WWT.

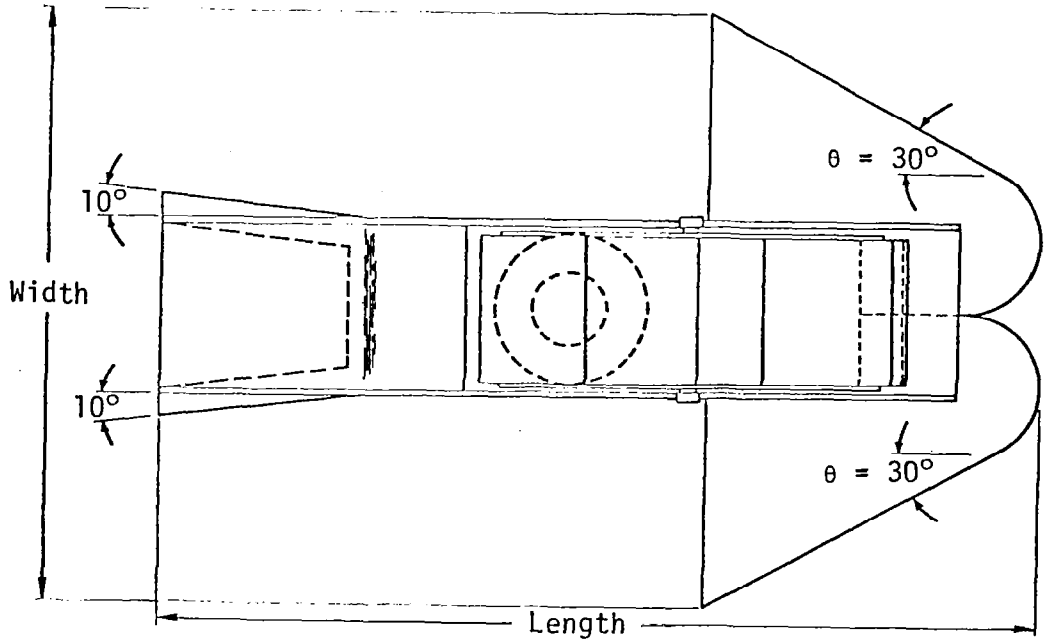

Figure 3 Top view of WWT.

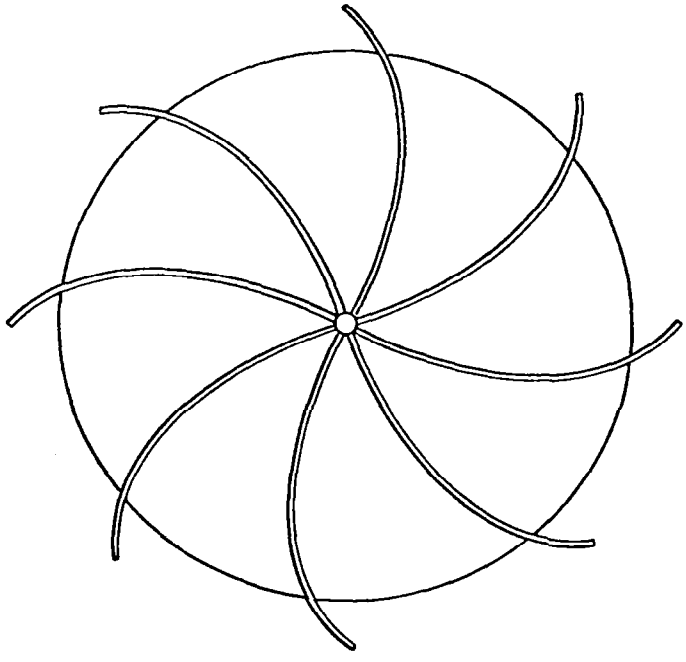

Figure 4 Illustration of wheel of the WWT.

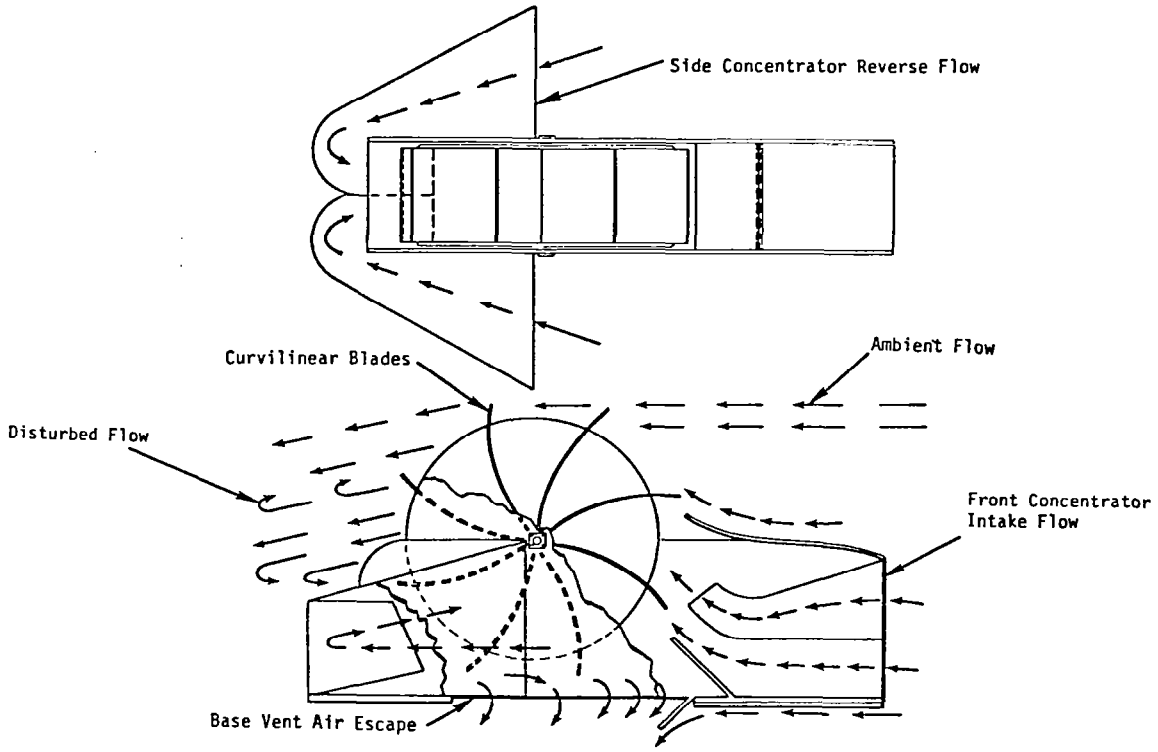

Figure 5 WWT internal/external airflow.

It is generally concluded that without reaction blading a turbine of this type has the characteristic that the moving surface must always travel at a lower speed than that of the wind. The speed of revolution of the rotor is thus low, resulting in the need for a step-up gearbox when a high-speed electrical generator is to be driven. Analysis suggests that rotational speeds on the order of 25 to 30 rpm can be achieved, which is not appreciably less than that of existing wind energy systems.

Two preliminary experimental studies of the wind-wheel concept have been carried out. Photographs of a paper model, Model #1, and of a stainless steel model, Model #2, are shown in Figures 6 and 7. Also, an analytical model has been developed and performance characteristics computed.

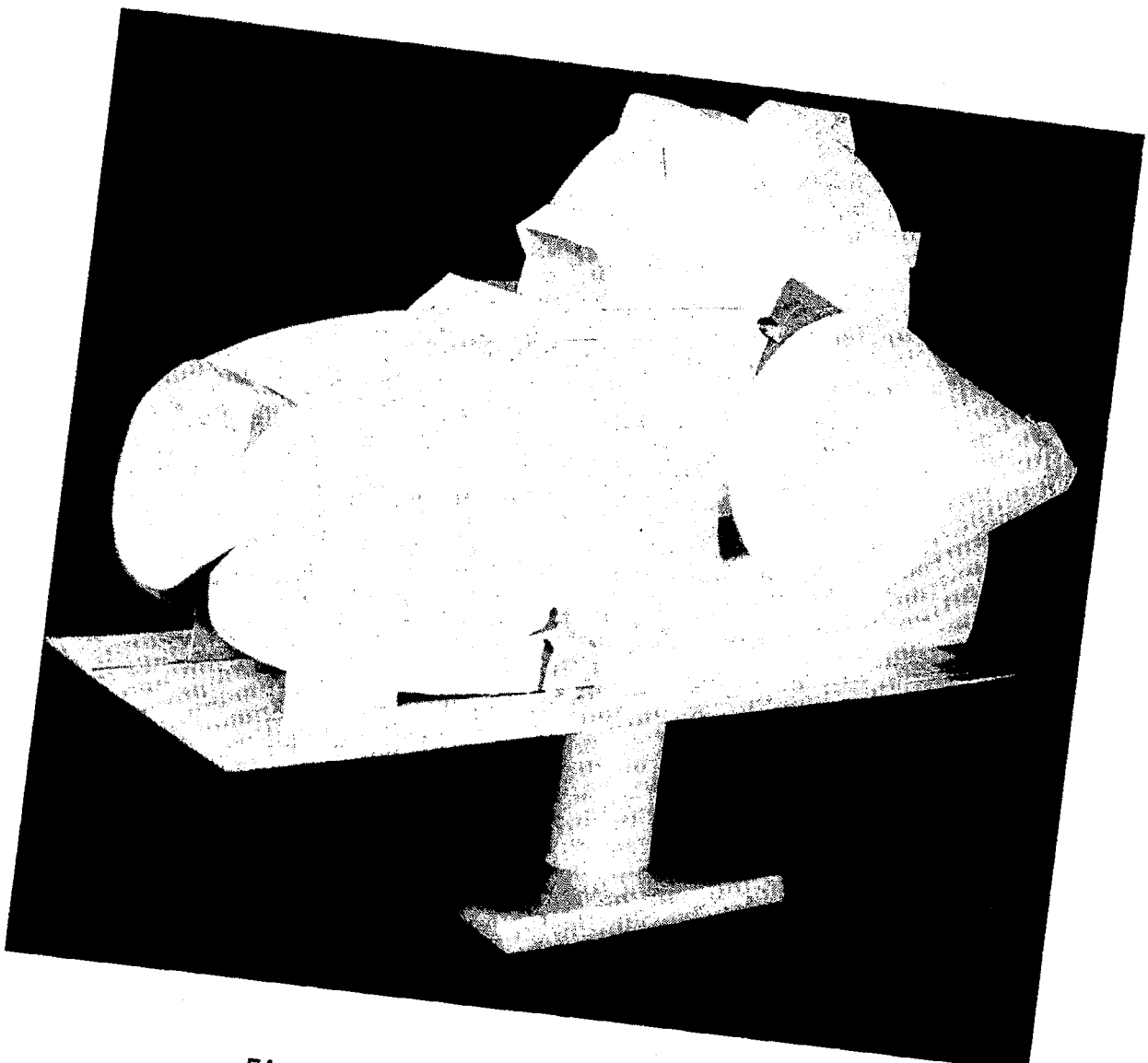

Figure 6 Model #1 of the WWT.

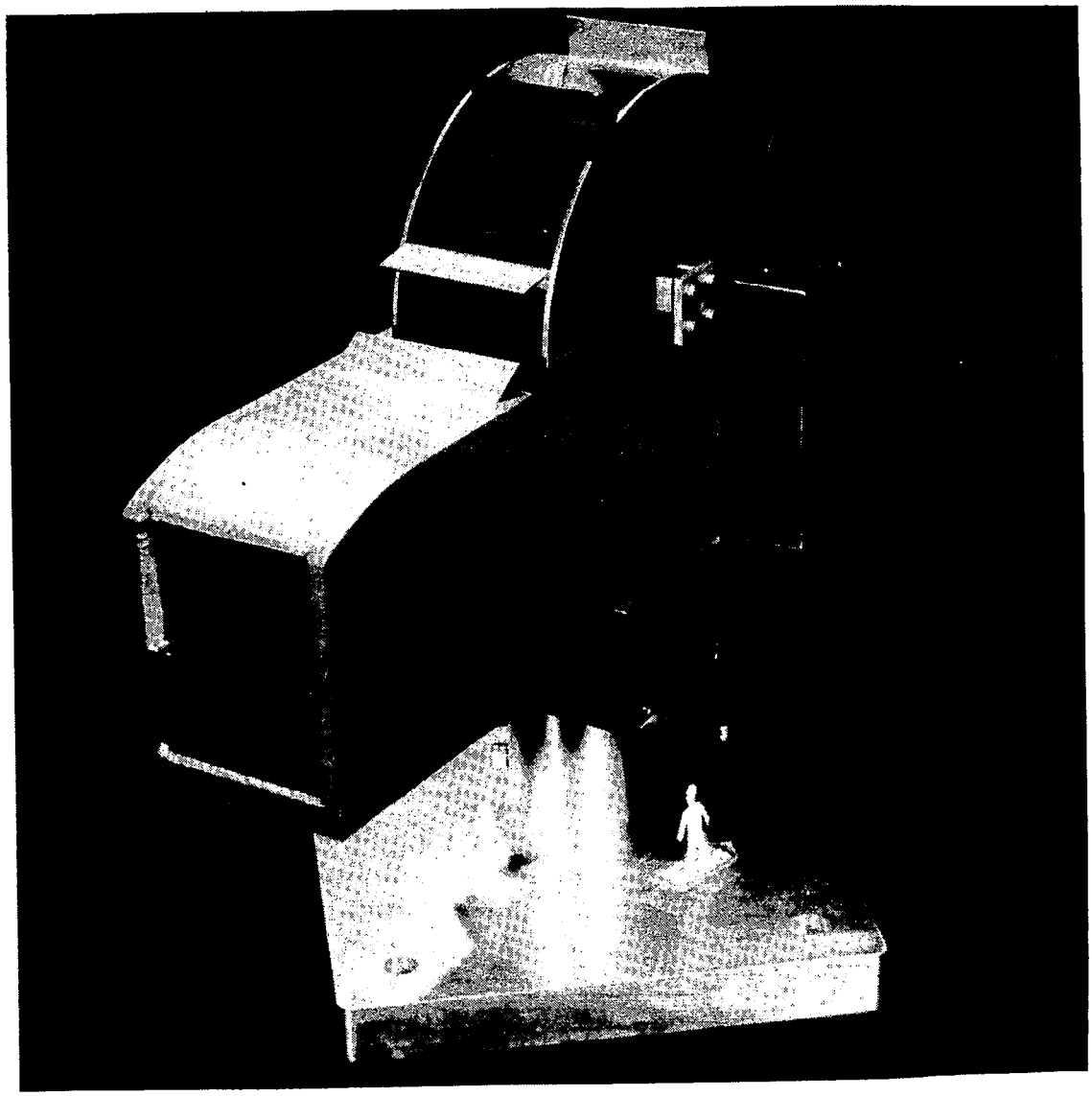

Figure 7 Model #2 of the WWT.

2.0 EXPERIMENTAL STUDIES

A series of preliminary tests on two models, which were not exactly to the scale proposed in the preceding, were carried out. These tests were made without funding and were in a sense a "makeshift" experiment. However, they have provided useful information that does demonstrate potential for the WWT. The results of these tests are described in the following paragraphs. First, a description of Model #1 and test results are given. Model #2 is then described and its preliminary performance verification discussed.

2.1 WWT Model #1 Design and Test Results

Model #1 of the WWT (Figure 6) is made of paper and pasteboard. The only metallic parts of the model are two small bearings and a metal axle. The model stands approximately 36 cm (14 in) high. The disks on the side of the wheel have a diameter of 15.24 cm (6 in). The blades extend 0.95 cm (0.375 in) beyond the outer circumference of the outer wheel disks. The blades are 6 cm (2.36 in) in width and join at the small center axle point. The model is not to scale with respect to shape and size of the ducts, wheel, main housing, and other features.

Limited testing of the paper model was carried out at low-speed airflow conditions. The model was exposed to airflow ranging from 1.7 to 2.9 m s^{-1} where the air source was an overhead air-conditioning ventilation system. The flow was measured repeatedly during the tests by an anemometer manufactured by Hastings-Raydist, Inc., Hampton, Virginia. Figure 8 shows the number of WWT wheel revolutions per minute versus various exposure-geometry conditions. These WWT test conditions were: (1) all ducts open with airflow directed onto the front of the WWT system; (2) the front ducts were covered with a fitted piece of construction paper; (3) all ducts (front and side) were covered to allow no air to flow into the ducts; (4) all ducts were open (uncovered) and a hood made of construction paper was placed over the top half of the exposed wheel, allowing no air to flow directly onto the upper part of

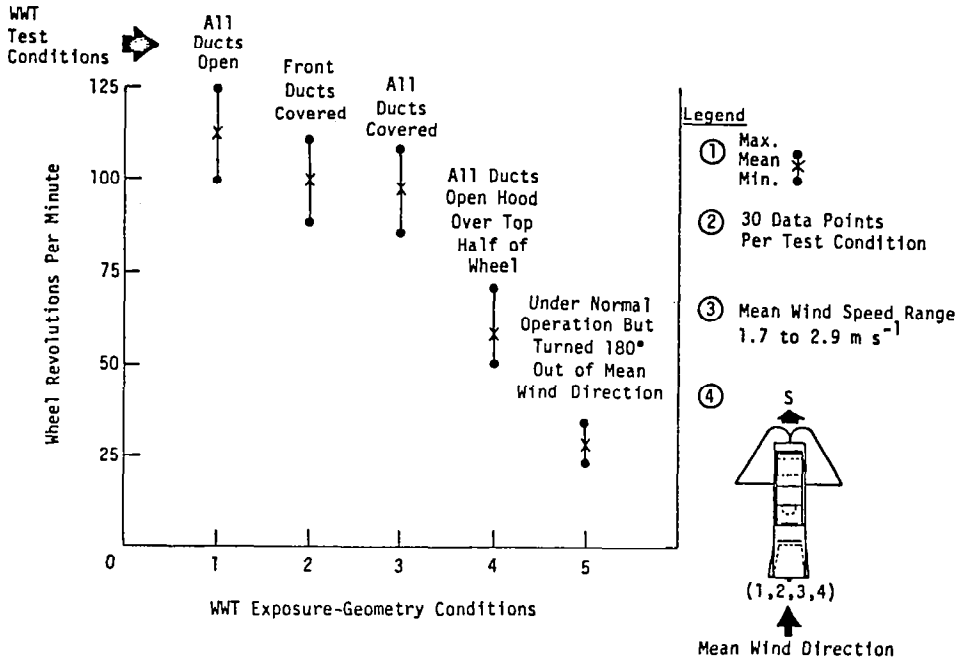

Figure 8 Revolutions of WWT (Model #1) wheel per minute versus various exposure-geometry conditions.

the wheel; and (5) the WWT Model #1 was turned 180° with respect to the mean wind direction. For each test condition, 30 one-minute samples of data were recorded. The number of revolutions were determined by counting the number of times an ink spot, marked on the outer edge of the wheel disk, appeared for a one-minute time period recorded with an electronic stop watch (Cronus 3-S, manufactured by Cronus Precision Products, Inc., Santa Clara, California). The arithmetic mean values were computed and are shown in Table 1 and in Figure 8. Table 1 also includes the ratio of the mean number of revolutions per minute of the wheel operating in an "all-ducts-open" normal mode (Condition #1) to the remaining four modes. It is interesting that the wheel turns in a normal rotational manner when the WWT model is turned backwards into the mean flow but only at one-fourth of the rotational speed.

It is especially significant to note the improvement in performance due to the front ducts, although the advantage of the side scoop appears marginal. Careful design of these is expected to enhance their effects.

TABLE 1 Minimum Mean,* Maximum Number of WWT (Model #1) Wheel Revolutions Per Minute with Respect to Each Test Condition.

WWT Test Condition	Wheel (rpm)			Ratio
	Min.	Mean*	Max.	Mean of Test #1 / Mean of Each Other
1. All ducts open	101	112.6	125	1.00
2. Front ducts covered	87	98.2	110	1.15
3. All ducts covered	85	96.2	108	1.17
4. All ducts open, hood over top half of wheel	51	57.7	68	1.95
5. Under normal operation but WWT turned 180 degrees out of mean wind direction	24	29.2	34	3.86

*Arithmetic mean of 30 one-minute data values.

A special set of wheel speed data was acquired using Model #1 which provides additional information as to how the wheel turns as it is positioned differently in regard to the mean wind direction. Figure 9 shows the Model #1 wheel revolutions per minute versus orientation of the model to the mean wind direction. The mean wind speed was measured at approximately 2 m s^{-1} with a range of 1.5 to 2.4 m s^{-1}. Again, these wind speed measurements were made with the Hastings' anemometer in the same air ventilation situation as used to obtain the data for Table 1.

The model (with duct open) was turned 22.5° at a time to the mean wind direction to Position #9 where the model faced 180° out of the mean flow. Again, 30 one-minute samples were taken at each position or orientation point.

The data illustrated in Figure 9 show that the lowest number of wheel revolutions per minute was at the orientation of 112.5° to the mean wind direction. The interesting fact is that the wheel rotates regardless of its orientation to the mean flow. Also, the wheel rotates about four times faster when the WWT points into the flow than when it points 180° "out-of-phase" with the flow.

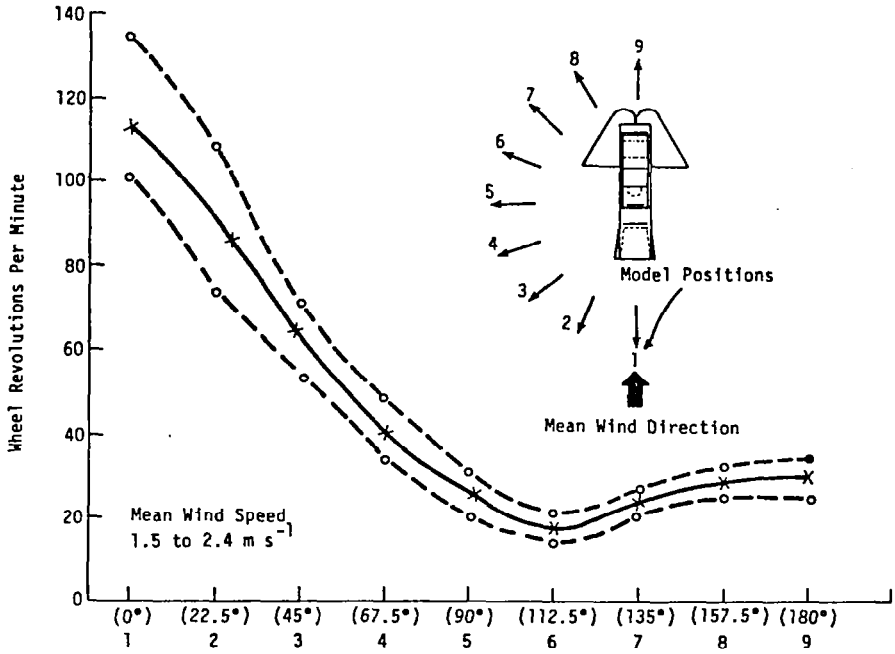

Figure 9 WWT Model #1 wheel revolutions per minute versus orientation to mean wind direction.

2.2 WWT Model #2 Design and Test Results

The stainless steel WWT Model #2 is shown in Figure 7. Again, the model is not built to the presently conceived proportions.

A laboratory experiment was conducted with this model. Figure 10 shows the basic equipment used to gather wheel spin-up, spin-down, and steady-state revolution data. The stop watch (Cronus Electronic Model 3-S) and hand-held anemometer (Belfort Instrument Company, SM-C-367329) are not shown in Figure 10. The electronic counter was a Hewlett-Packard 5245L unit, the airflow meter was Parker-Hannifin, and the other apparatus consisted of standard laboratory items. A photocell pulse detector was made from off-the-shelf electronic components. After several trials to determine airflow speed, placement of the air source with respect to the model, stability in acquiring accurate revolutions of the wheel with time, etc., the experiment was conducted. It should be mentioned that the air pressure remained very stable throughout all testing, which made the results more accurate. To determine airflow speed (wind speed in the figures to be discussed), the hand-held

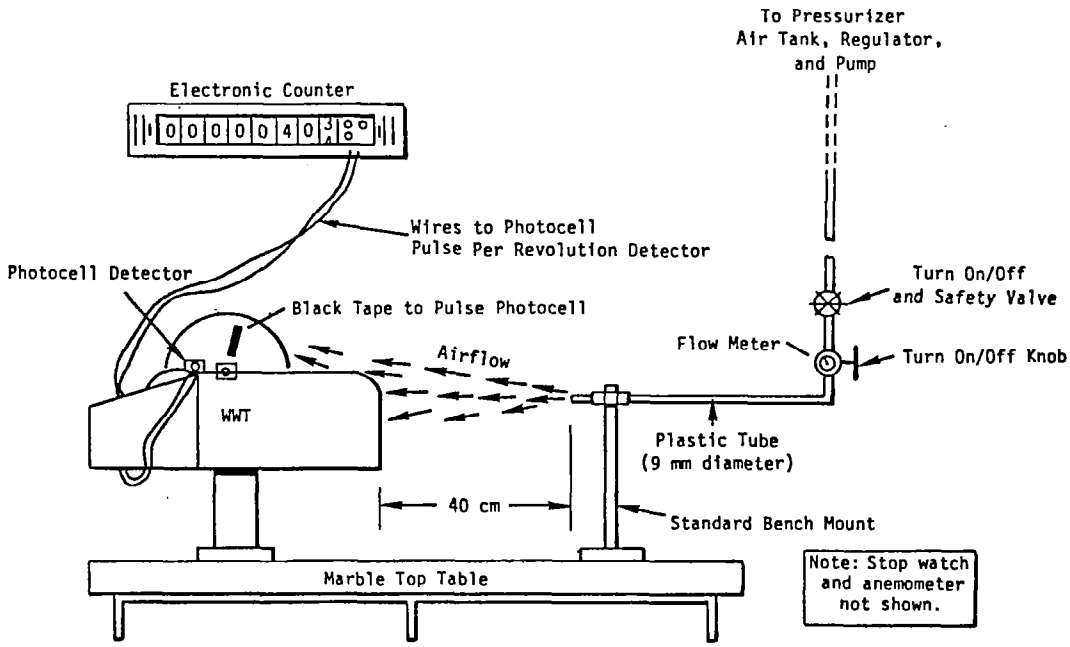

Figure 10 Laboratory apparatus used to obtain spin-up, spin-down, and steady-state WWT (Model #2) wheel pulse per revolution data.

anemometer was positioned approximately 40 cm away and directly in the mainstream of the jet (plume) of air. Measurements were made just prior to and after recording all data sets, and especially for similar groups of wheel turn data. To obtain the anemometer measurements, the air source was turned into the "open room" and measurements were not taken in front of or in line with any nearby obstacles. The laboratory air temperature remained approximately 25° C (78° F) throughout the testing.

2.2.1 Model #2 Performance Data Acquisition. Model #2 is made of stainless steel (Figure 7). The overall weight of the model is approximately 18 kg (40 lbs). It stands 35 cm (14 in) high, has a wheel that weighs approximately 2.25 kg (5 lbs), a blade length (i.e., radius of wheel) of 10 cm (3.9 in), a blade width of 6 cm (2.4 in), and an axle of 0.7 mm in diameter. The wheel bearings were made by the Fafnir Bearing Company, New England, Connecticut.

Three sets of data were acquired to determine the basic performance of the Model #2 wheel. These were spin-up, steady-state, and spin-down data. First, the wind speed required for the wheel to complete 20, 40,

and 60 revolutions starting from rest and as a function of mean wind speed (actually a jet or plume of air from a pressurized tank and nozzle) was determined. Figure 11 shows the raw data and fitted curves for these three conditions as well as the threshold start or breakaway speed of 3.1 m s^{-1}. As can be seen on the ordinate of Figure 11, it requires approximately 30 seconds in a 4 m s^{-1} mean wind speed to cause the wheel to rotate 20 times; whereas, it only takes 10 seconds for the wheel to rotate 20 revolutions in a 16 m s^{-1} mean wind speed.

The steady-state rotational speed data and curve fit are shown in Figure 12. These data show the wheel revolutions per minute as a function of steady-state wind speed. The wheel threshold speed of 3.1 m s^{-1} is also shown; however, the wheel rpm values are only given to about 650. The reason higher rpm values were not obtained for winds above 10 m s^{-1} was to avoid ball bearing heating.

The third set of data consists of the wheel stop time or spin-down data. The data and curve fit are shown in Figure 13. It is interesting

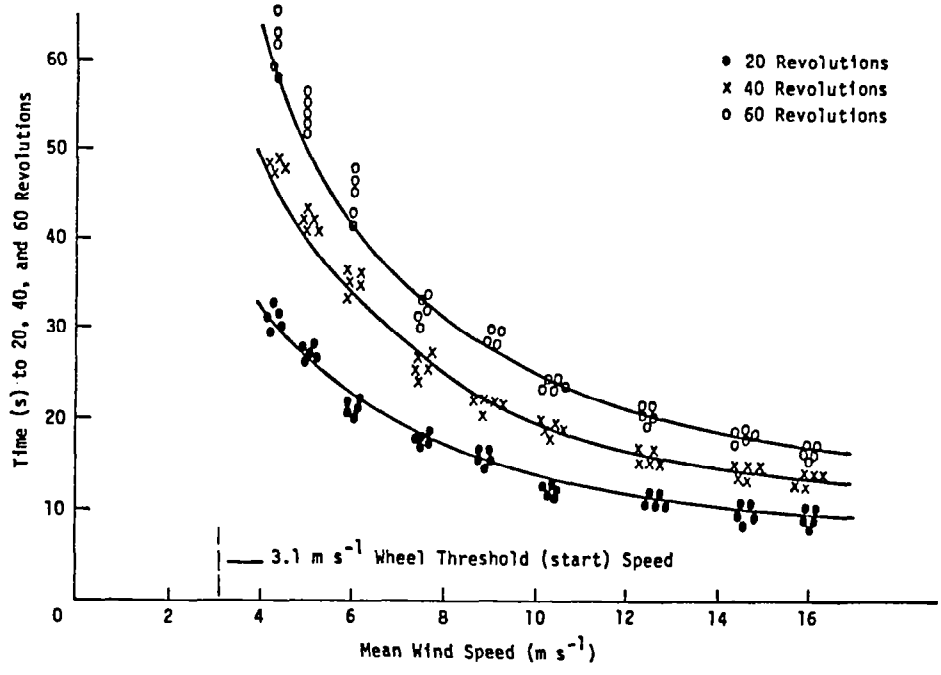

Figure 11 WWT wheel time to reach 20, 40, and 60 revolutions versus mean wind speed (Model #2).

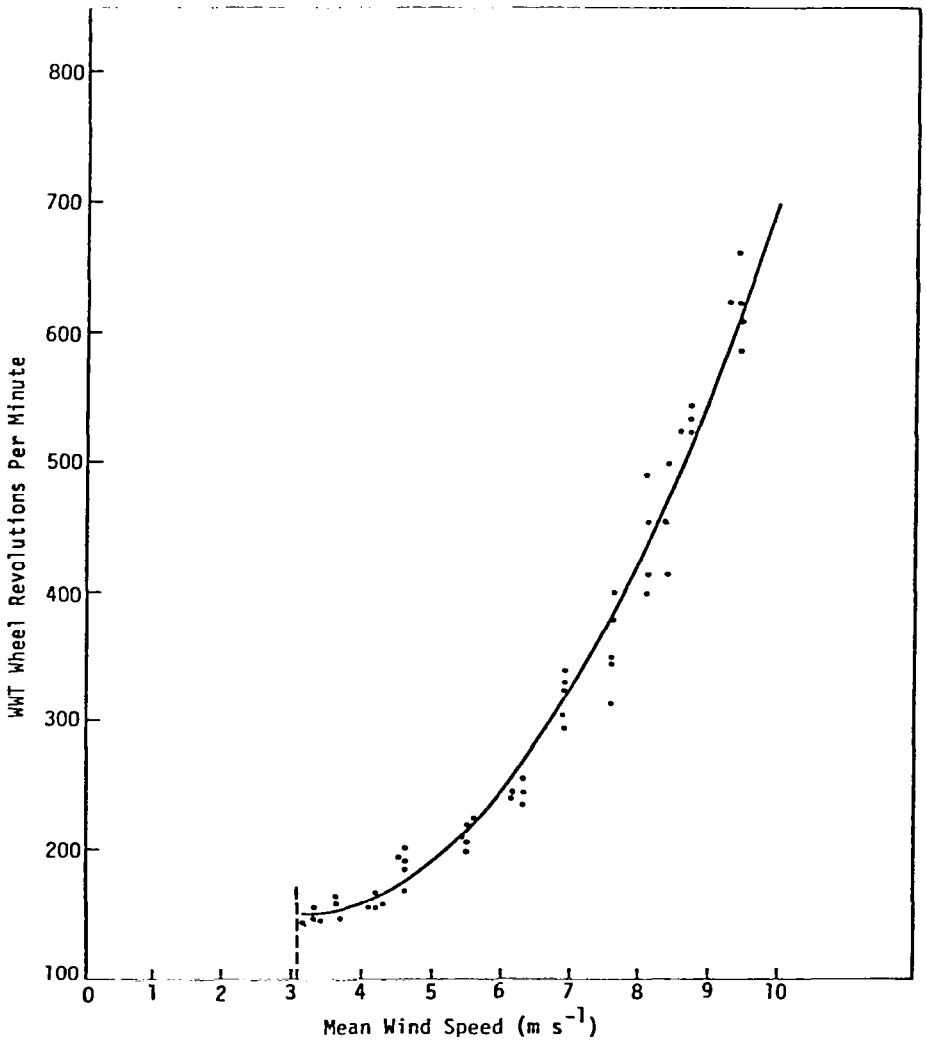

Figure 12 WWT wheel revolutions per minute versus mean wind speed (Model #2).

to note the appreciable difference in wheel slowdown time versus rpm. As shown, it takes approximately 500 seconds for the wheel to stop if it is given a constant rpm of 500, compared to approximately 400 seconds to stop when at a speed of 150 rpm. This indicates that the wheel has a very significant drag force to still air when rotating at high speeds.

2.2.2 Analyses of WWT Model #2 Performance Data. The performance of the WWT model can be estimated from the experiment observations in a straightforward manner. The torque, T, power, P, and coefficient of

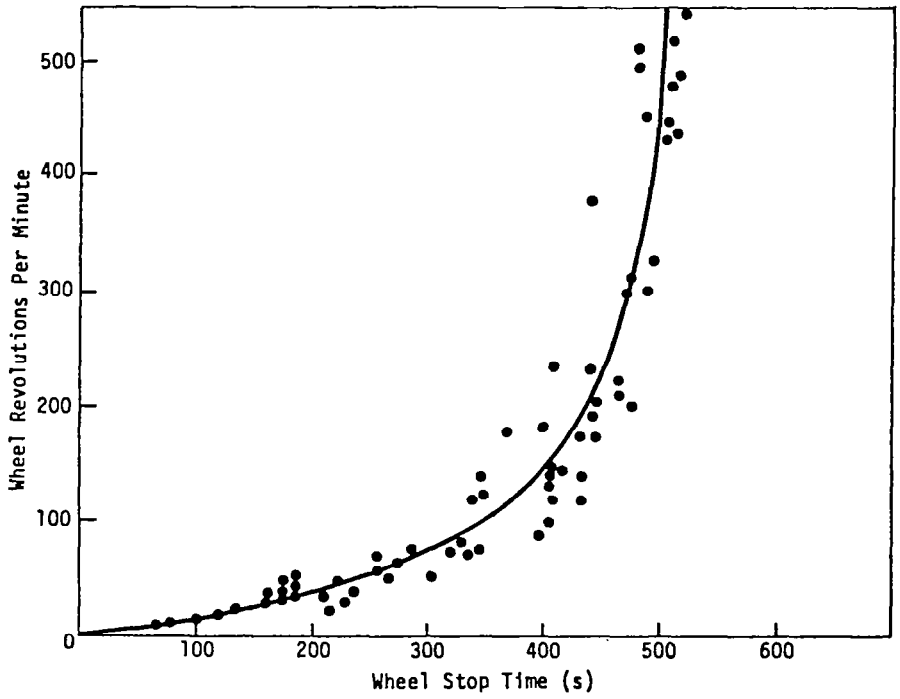

Figure 13 WWT wheel initial revolutions (turn speed) versus stop time (Model #2).

performance, C_p, for the WWT can be calculated from:

$$T = I\alpha \tag{1}$$

$$P = \omega T = \omega I\alpha \tag{2}$$

$$C_p = \frac{P}{\frac{\dot{m}V_1^2}{2}} = \frac{2I\alpha\omega}{\rho A V_1^3} \tag{3}$$

where θ, ω, and α are the wheel angular position, velocity, and acceleration; ρ, $\dot{m}$, and V are the air density, mass flow rate, and velocity; and I is the turbine wheel moment of inertia. The experimental data of Figure 12 were least squares curve fit to the relation:

$$\theta = \frac{-a_1}{a_3^2} + a_2 t + \frac{a_1}{a_1} e^{-a_3 t} \tag{4}$$

The form of Equation 4 was chosen to produce the proper functional relationships at t = 0 and t = ∞ and substituting in Equation 3 yields

the following:

$$C_{p_{max}} = \frac{I}{2\rho A V_1^3} \alpha_o \omega_\infty^2 \qquad (5)$$

All of the variables in Equation 5 can be deduced from the test data taken except the capture area, A. Since the capture area was not measured, an approximate capture area of 75 percent of the WWT wheel peripheral area was used to calculate the values of power coefficient shown in Table 2.

TABLE 2 Values of Power Coefficient Calculated from the Second WWT Model Test Data.

V (m/s)	4.328	10.370	15.835
C_p	0.620	0.327	0.206

These data show the WWT to be relatively efficient at low wind speeds and inefficient at high wind speeds. This behavior is a strong function of blade and flow passage geometry since a properly designed turbine should produce power coefficients near 0.85 (based on the actual mass flow rate) when operating at the design point for any reasonable design wind speed.

The data from Figure 13 were investigated. It was determined that the largest portion of the decelerating force varied as a function of the square of the rotational speed which is what is to be expected for windage and pumping losses. A small amount of frictional drag is apparent from the wheel behavior below 100 seconds. This drag dramatically shortens the coast-down time but is not significant at higher rotational speeds.

Results of this study, although very preliminary, do illustrate that the device has potential and that the system is a viable technique for converting the kinetic energy of the atmospheric wind into rotational energy.

3.0 ANALYTICAL STUDIES

3.1 Performance Prediction Techniques

The detailed performance analysis of the WWT is difficult since the WWT, as presently configured, does not fit into any one classical pattern. The device behaves somewhat like a simple water-paddle wheel and somewhat like an impulse gas turbine. A complete performance analysis of the WWT must consider the interaction between the inlet flow, the turbine wheel blade flow, and the turbine outlet flow.

A preliminary analysis of the WWT performance, based on a simple engineering model described in the appendix, was carried out. Figure 14 schematically illustrates the model. Only four blades are considered for simplicity; however, this is not expected to be the optimum number. The engineering model is represented effectively by three jets of wind acting on the turbine rotor. Jet 1 is the freestream wind speed, V_1; jet 2, resulting from the front duct concentrator, has a speed of V_2; and jet 3, resulting from the side scoops redirecting the flow onto the backside of the turbine rotor, has a speed of V_3. The front duct will be constructed with a contoured configuration which will accelerate the flow. The acceleration is expressed by the ratio $\zeta_2 = V_2/V_1$. Although detailed calculations are needed to determine the magnitude of ζ_2, it is estimated that values between 1 and 2 are realistic. When $\zeta_2 = 0$, the duct is closed.

Similarly, the velocity of flow impinging on the rear side of the blade from duct 3 is less than the freestream velocity due to the deceleration caused by turning through 180°. This deceleration is represented by $\zeta_3 = V_3/V_1$. To assign a specific value to ζ_3 also requires detailed analysis; however, ζ_3 will be less than unity and is estimated to lie between 0.1 and 0.5. Again, $\zeta_3 = 0$ represents a closed duct.

Forces due to all three jets acting on the rotor create a torque which is expressed in coefficient form as:

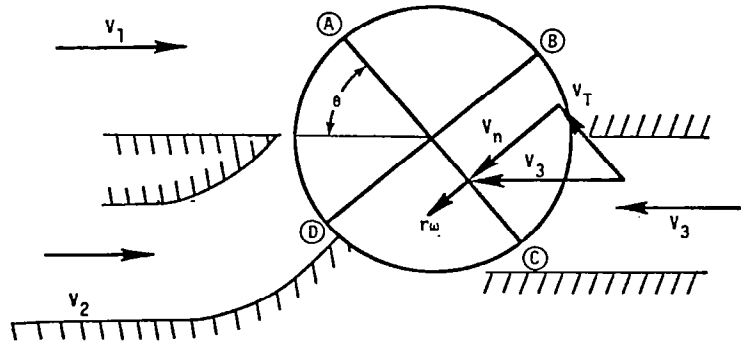

Figure 14 Definition of jets and blade interaction.

$$C_T = 2 \text{ Torque}/\rho w R V_1^2 \tag{6}$$

where ρ is the density of the air, R is the radius of the rotor, w is the width of the wind turbine wheel, and V_1 is the freestream wind speed.

The power coefficient of the WWT is then related to the torque coefficient by the relationship (see appendix, Equation A-6):

$$C_p' = \lambda C_T \tag{7}$$

where λ is the ratio of tip speed to freestream wind speed (i.e., $\lambda = \omega R/V_1$) and ω is the rate of the angular rotation of the wind turbine wheel. The C_p' given by Equation 6 is based on a flow area of wR. However, the actual area of the wind flow entering the various ducts is estimated as approximately 3.3 wR. Hence,

$$C_p = C_p'/3.3 \tag{8}$$

Values of C_p reported throughout this section are, therefore, based on an effective area of $A_e = 3.3$ wR.

Computed values of C_p computed for the wheel at the angular position of $\theta = 45°$ (see Figure 14) for given values of the tip speed ratio are shown in Figure 15. This figure illustrates the influence of the front duct venturi, which produces a significant increase in the C_p values. These values of C_p are thus competitive with conventional propeller-type wind turbine generators. The influence of the air drawn

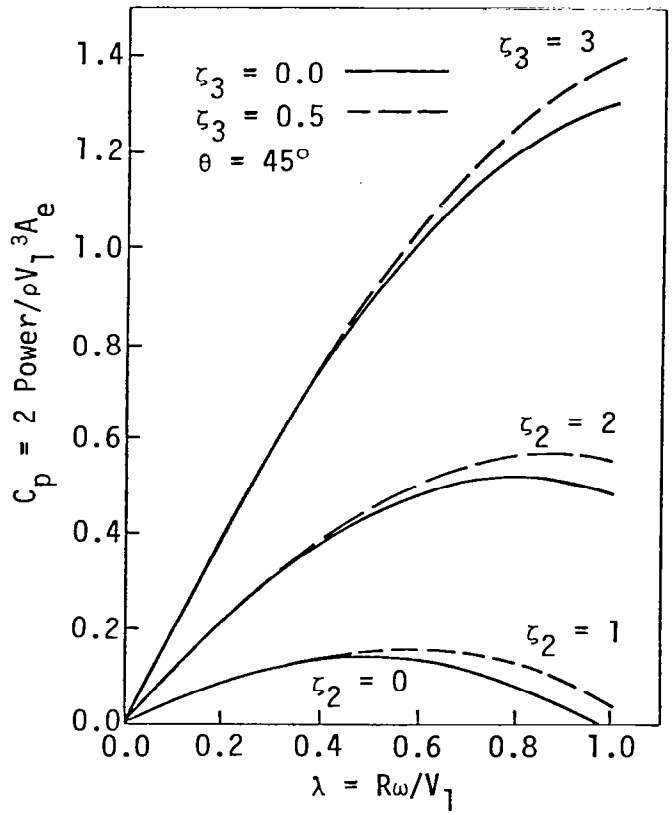

Figure 15 Computed influence of accelerated flow through front duct.

in through the side scoops is relatively small is also indicated in the figure. Therefore, throughout the remainder of this section, a value of $\zeta_3 = 0.1$ has been used. It is anticipated that through careful design of the front venturi duct, values of $\zeta_2 = 2$ can realistically be obtained.

Figure 16 shows how the value of C_p varies with rotor angular position. The data are plotted only for θ ranging from 0° to 90° since a four-bladed rotor C_p varies cyclically with a period of 90°. The nonuniformity of C_p with angular rotation can be reduced by utilizing additional blades on the wind turbine wheel.

It should be noted that low tip speed ratio devices such as the WWT generally have high coefficients of torque associated with them. Figure 17 illustrates the starting coefficient of torque for various values of acceleration through the front concentrator. The starting torque is very high and demonstrates a good characteristic of the system for applications to pumping and other mechanical subsystems requiring high torque.

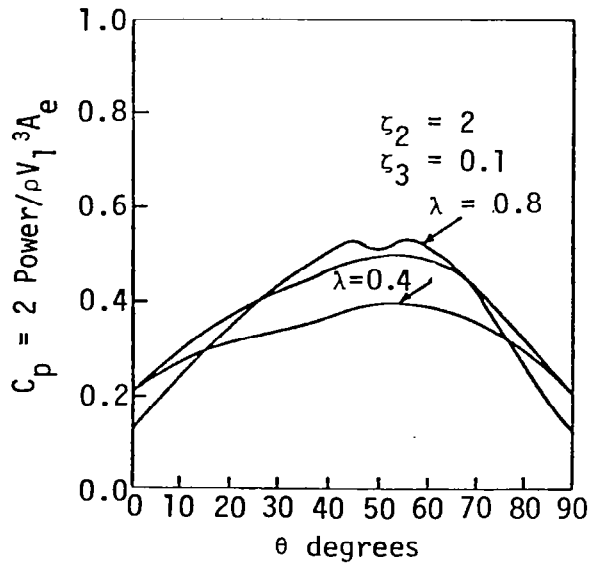

Figure 16 Computed variation of the power coefficient with rotor position.

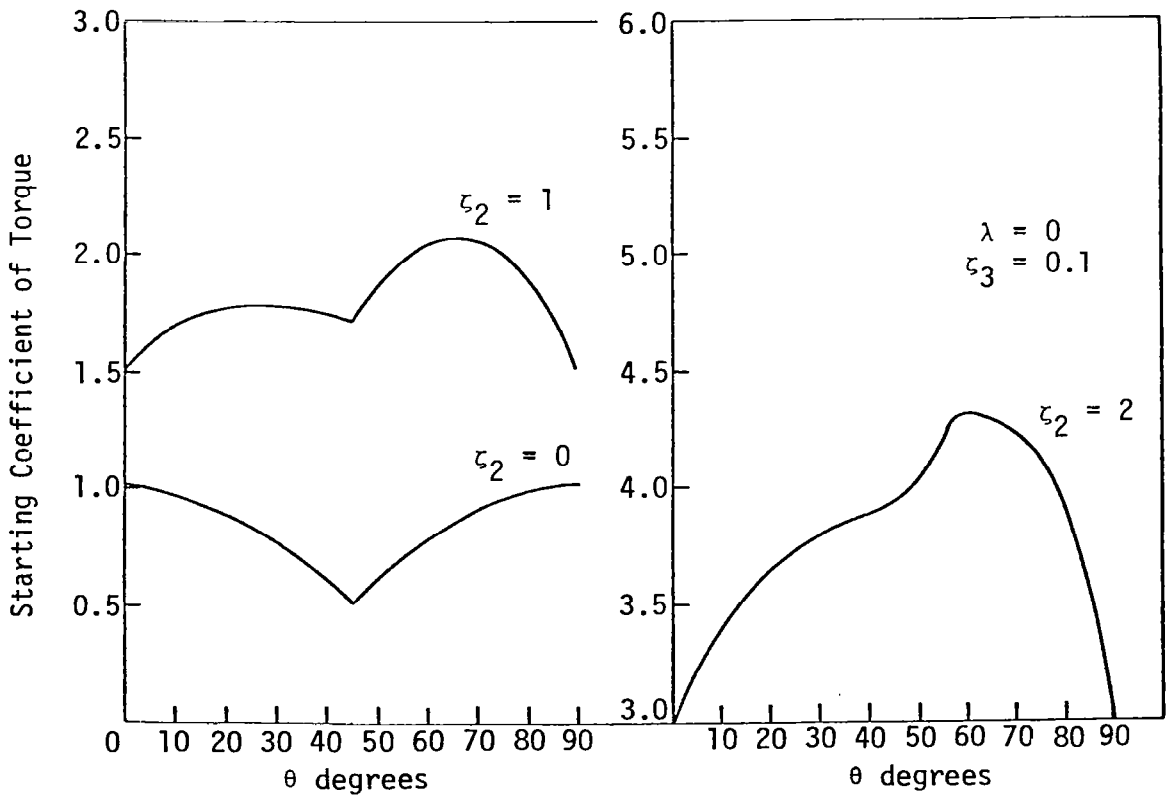

Figure 17 Computed influence of flow through front duct on starting torque.

Figure 18 illustrates how the torque varies on an individual blade throughout a complete 360° rotation. Relatively high cyclic loading occurs which will be a fatigue factor that must be carefully considered in the blade design. This cyclic loading, however, is no greater than that of a conventional propeller rotor. Moreover, the wind turbine wheel will be less susceptible to high fatigue moments because of the sturdier construction of each blade as contrasted to the cantilever construction of propeller-type rotors.

A comparison of the performance of the WWT relative to other systems is shown in Figure 19. The shaded area illustrates the range of C_p's that is potentially achievable from the innovative system. Although careful study is required to verify the exact curve, the WWT is competitive in terms of C_p coefficients for other systems.

The analysis given in the appendix includes several simplifying assumptions that must be relaxed for a more rigorous analysis. For example, the flow over the blades requires a momentum balance rather

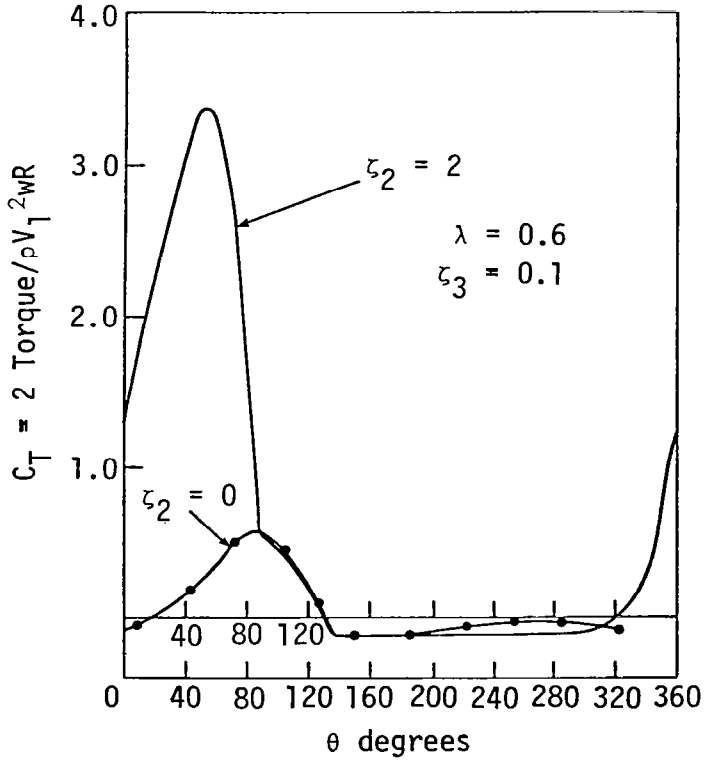

Figure 18 Influence of front concentrator on torque of individual blade.

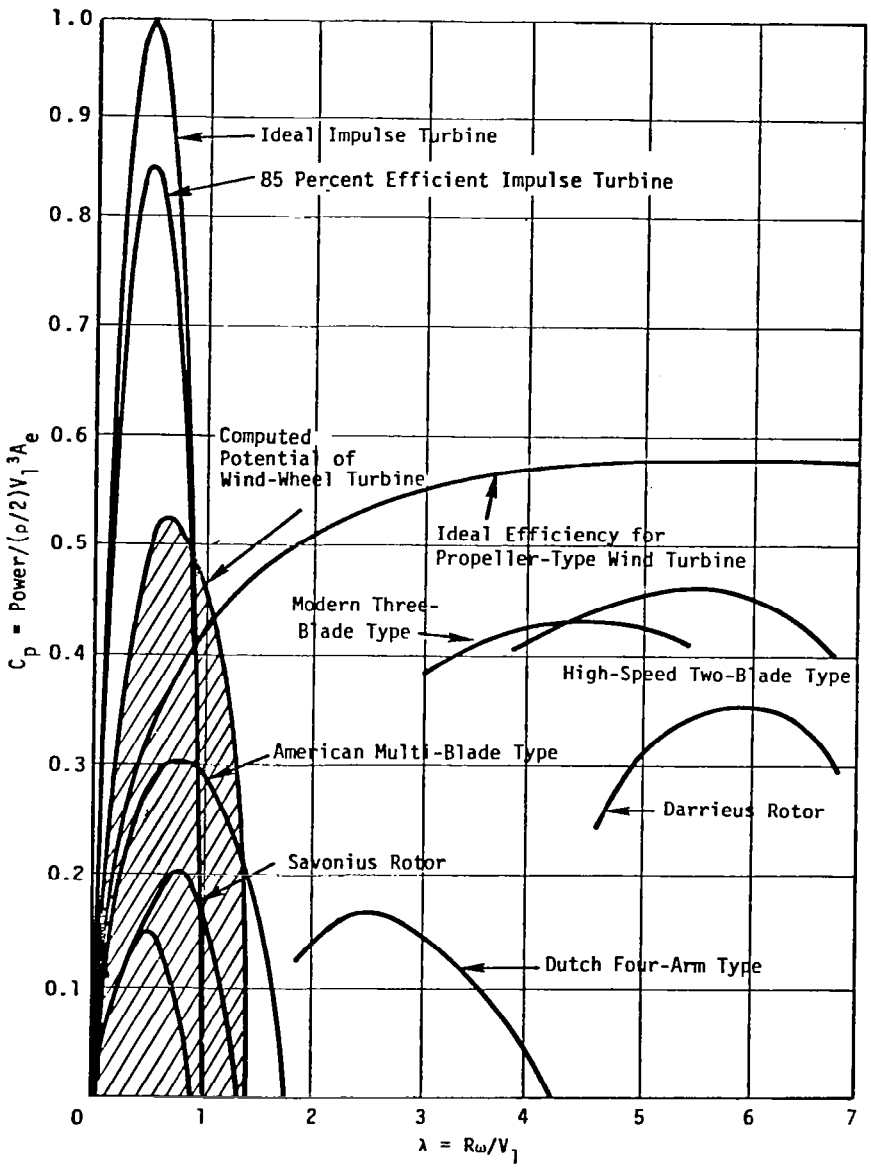

Figure 19 Comparison of the performance of several wind machines.

than simply relating force to the square of the relative velocity. The momentum balance will indicate the momentum loss due to escaping air and thus define the required exhaust ports. Figure 20 illustrates some simple concepts for reducing the back pressure on the airflow while retaining the major portion of the momentum for transferring force to the blade.

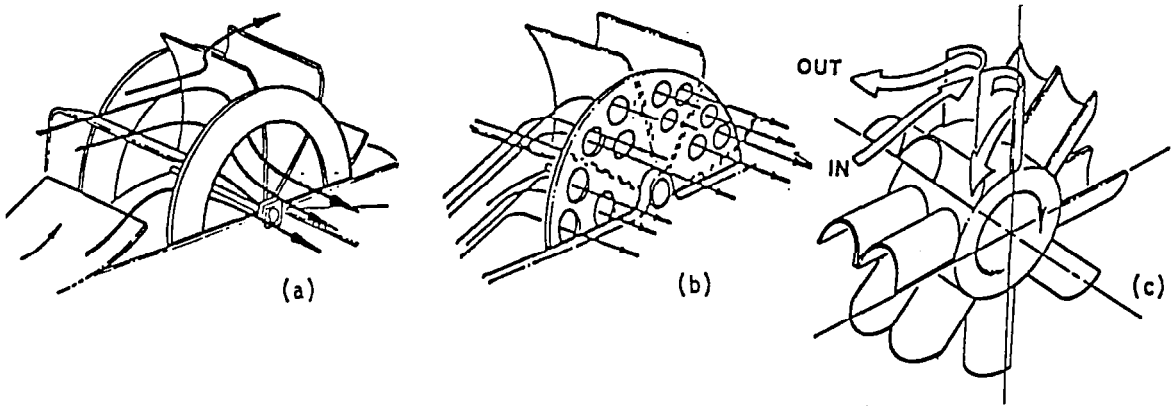

Figure 20 Concepts for exhausting airflow.

Boundary layer effects must also be considered. These will result in additional loss of momentum on the blade due to friction forces. The boundary layer build-up and the momentum transfer will then identify the optimum blade configuration required to provide the most efficient flow and thus transmit the highest force possible. Boundary layer analysis must also be applied to the friction drag created by the fluid flow between the plate and the supporting walls. This analysis will indicate the optimum distance between the rotating wheel and the supporting side walls.

3.2 Inlet Duct Analysis

The inlet duct analysis of an existing device should predict the gross flow of the air in the ducts as well as identify problem areas such as boundary layer blockage and separation. The one-dimensional flow assumption is a good first approximation, and laminar or turbulent boundary layer blockage can be approximated by use of the semi-empirical relations found in Reference 1. The blockage problem can be treated by adding the boundary layer displacement thickness to the required ducting inviscid contours. One method of treating boundary layer separation is to bleed a small amount of low-energy boundary layer air from the inlet duct. This causes an additional drag load on the WWT assembly which must be resisted by the tower and also requires the inlet ducts to be slightly larger than would be otherwise necessary but results in increased power for a fixed size wind turbine wheel.

3.3 Turbine Blade Analysis

The Euler turbine equation, taken from Reference 2, which describes the energy, E, that can be extracted from a unit mass is applicable to both the impulse and reaction turbines:

$$E = \frac{1}{2}\left[(V_1^2 - V_2^2) + (U_1^2 - U_2^2) + (V_{r_2}^2 - V_{r_1}^2)\right] \tag{9}$$

where V is the absolute velocity, V_r is the velocity relative to the blade, and U is the blade velocity. The subscripts 1 and 2 refer to the inlet and outlet. The turbine geometry is shown schematically in Figure 21. The performance of the WWT model could be estimated using the Euler equation if sufficient information had been gathered concerning the geometry of the flow path into and out of the turbine wheel. The degree of reaction is defined as:

$$R = \frac{\frac{1}{2}\left[(U_1^2 - U_2^2) + (V_{r_2}^2 - V_{r_1}^2)\right]}{E} \tag{10}$$

If the variation in radius is ignored so that $U_1 = U_2$, the degree of reaction is seen to be a measure of how much of the available energy extraction is associated with a kinetic energy change of the working fluid in the rotor. For $V_{r_1} = V_{r_2}$, R = 0 and we have an impulse turbine. The impulse turbine is important because it is the only class of turbine in which there is no static pressure change in the rotor; hence, the rotor may be open, i.e., no side walls. Pelton wheels and paddle wheels are impulse turbines; the first having a high efficiency, the second a low efficiency.

An advantage of using the Euler equation to help design the WWT blades as impulse blades is that we can easily see how the blade properties affect performance. The velocity diagram approach can be used to suggest improvements to the current WWT design and to illuminate the limitations imposed by gas dynamics upon the maximum tip speed ratio and wind concentration factor of an impulse-type turbine. The impulse turbine simply turns the flow as much as possible to extract as much energy from each pound (kilogram) of flowing gas as is possible and

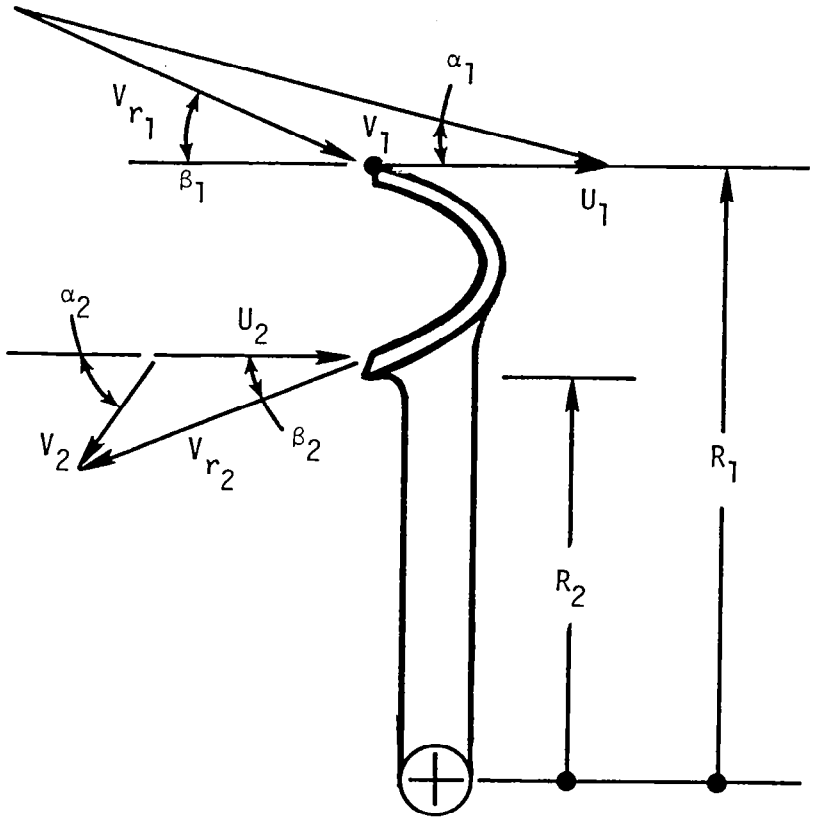

Figure 21 General impulse turbine blade nomenclature.

still manage to pass the efflux out of the turbine exit. Properly designed, impulse turbines are extremely efficient in terms of extracting the energy from the gas. Considering the blade force, F_b, and power, P:

$$F_b = \dot{m}(V_1 \cos \alpha_1 - U_1 + \cos \alpha_2 V_2 + U_2) \tag{11}$$

$$P = \dot{m}\omega(V_1 \cos \alpha_1 - U_1)R_1 + (V_2 \cos \alpha_2 + U_2)R_2] \tag{12}$$

or

$$P = \dot{m}[V_1^2 \cos^2 \alpha_1(1 - \lambda)\lambda + U_2(\cos \alpha_2 V_2 + U_2)] \tag{13}$$

where λ is the tip speed ratio V_1/U_1. Ignoring the exit energy temporarily, it can be shown that the power coefficient:

$$C_p = \frac{P}{\frac{\dot{m}V_1^2}{2}} = 2 \cos^2 \alpha_1(1 - \lambda)\lambda \tag{14}$$

can be maximized by setting $\alpha_1 = 0$ and $\lambda = 0.5$. The fact that the C_p approaches 1 as the total power approaches 0 is somewhat discouraging but expected since:

$$P = 2\pi\rho W V_1^3 R_1 (1 - \lambda)\lambda \sin \alpha_1 \cos^2 \alpha_\alpha \quad (15)$$

An alternate approach is to maximize the power for a given turbine wheel regardless of the resulting power coefficient. This would tend to maximize the return on investment in the expensive rotating parts. This can be achieved by maximizing the $\sin \alpha_1 \cos^2 \alpha_1$ term in Equation 15 which results in an optimum $\alpha_1 = 35.26°$.

A comparison of the power obtained at 35° inlet angle to that obtained at some lower angle such as 12° shows that the same diameter turbine will produce 1.95 times the power with the blades configured for a 35° entry angle than for a 12° entry angle. The 35° blade configuration loses approximately 18 percent in efficiency (C_p) but gains by a factor of 2.77 in flow rate. The 35° entry angle will produce a larger turbine exit velocity than the 12° configuration. This lost kinetic energy can be utilized to energize the exit duct flow to increase turbine inlet velocity by use of a turbine exit diffuser as discussed in Section 3.4.

Of course, the flow in the existing MSFC WWT is not two-dimensional. The WWT turbine wheel could be modified to turn the flow as in a Pelton wheel as is shown in Figure 20. The Euler turbine equation could also be used to evaluate the performance of such a device with good accuracy if the exit flow path could be estimated or measured.

In any case, the important consideration in turbine design is to make provisions for the turbine outflow air so that it may move smoothly into the exhaust duct or plenum.

3.4 Exhaust Considerations

As a first step in improving the WWT performance, it has already been suggested that the turbine wheel hub area be opened to allow the low-energy exhaust air to escape the turbine wheel as is shown in Figure 20. The flow of the exhaust gas must be modeled accurately to determine the full effect of exhaust restrictions on the WWT performance.

The application of inlet flow intensifiers to increase the performance of the wind turbine is dependent upon the use of some device to lower the turbine exit pressure. The actual benefit that can be derived from an intensifier is a function of the turbine exhaust duct geometry and location. This can be better understood by considering Figure 22. The air enters the inlet intensifier and is assumed to accelerate from velocity V_1 to V_2, the velocity ratio being controlled by the area ratio. The resulting C_p increases by the ratio of $(V_2/V_1)^2$.

$$C_p = \frac{2\dot{m}V_2^2(1 - \lambda)\lambda}{\dot{m}V_1^2} = 4(1 - \lambda)\lambda \frac{V_2^2}{V_1^2} \tag{16}$$

The air pressure in the inlet duct decreases as the velocity increases since its total pressure is constant and remains constant, ideally, as it flows through the impulse turbine. If a constant area exhaust duct is used, the gas will be dumped at the exhaust duct exit at the same static pressure as exists at the exit of the inlet duct. Unless a deliberate effort has been made to locate the duct exit in a low

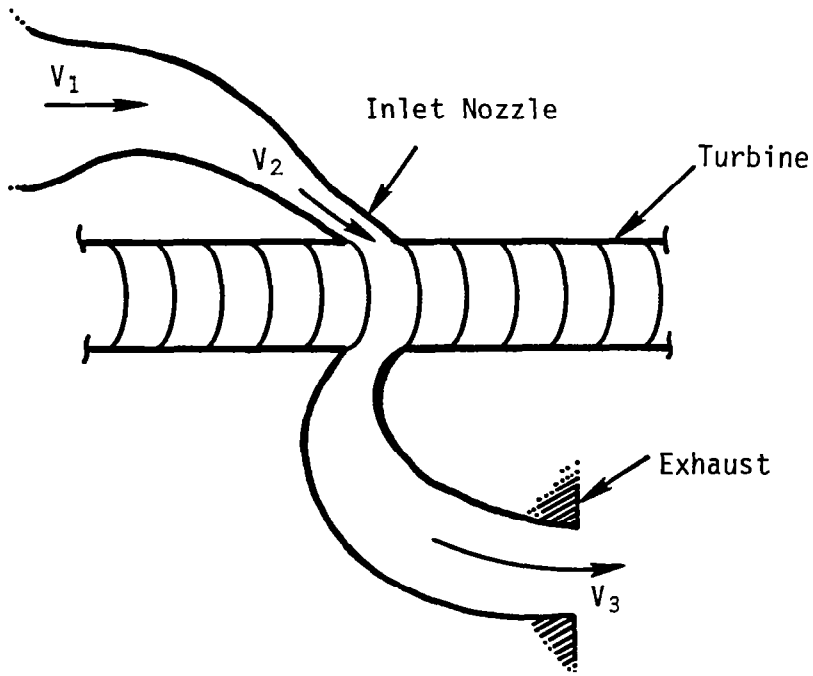

Figure 22 Impulse turbine exhaust effects.

pressure area, then $P_3 = P_1$ and the exhaust pressure is equal to the ambient static pressure. Thus:

$$P_1 = P_3 = P_1 + \frac{\rho}{2}(V_2^2 - V_1^2);\ V_2 = V_1 \tag{17}$$

Therefore, the turbine inlet velocity can be increased only if the exhaust duct static pressure is reduced or if an effective exhaust diffuser is used.

A low pressure area does exist in the lee of the flow behind the turbine housing. A review of the existing literature on base drag indicates that a base pressure coefficient as low as -0.5 has been obtained. Assuming the base pressure coefficient of -0.3 reduces the pressure by -0.3 times the dynamic pressure which propagates through the ducts and turbine as a turbine inlet velocity increase of:

$$\frac{V_2^2}{V_1^2} = \frac{C_p}{C_{p_o}} = 1.3 \tag{18}$$

Summarizing the above design discussion, the dimensions of the ducted wind turbine can be reduced by 28.1 percent while maintaining the same power output if the turbine inflow angle is optimized. Similarly, the use of exhaust diffusers and inlet flow intensifiers can increase the power coefficient by as much as 30 percent, which would allow an additional 12.3 percent reduction in linear size. Use of both of these options would produce a linear size reduction of 36.8 percent which translates into a surface area reduction of approximately 60 percent. Since surface areas are closely related to costs, it is obvious that the optimization of the WWT geometry can produce extremely significant results and therefore should be investigated thoroughly.

3.5 Other Design Considerations

The final WWT wheel design will be the result of a number of trade-off studies between the shape of blades, number of blades, the use of stator blades, size, etc. Variable pitch stator blades may be used to control the wheel speed to produce constant frequency (i.e., constant rpm) power even in high winds.

Components and subcomponents of the WWT must be sized so that they do not vibrate at matched frequencies. This will be easier to do for the WWT than for the propeller-type wind turbine since the WWT blade shape can be changed independently of the WWT wheel structural arrangement.

The WWT wheel bearings present a much simpler design problem than the bearing design for a propeller-type windmill. In its ultimate configuration as a 360° inflow turbine, the WWT blade forces will balance each other and exert only a torque on the wheel which in itself produces no load on the bearing. If the power is taken off at the wheel periphery by a belt or chain, this torque will impose a relatively low reaction force on the bearing due to the large radius. Calculations show that the bearings will have to react to the major load of the turbine wheel weight. There will be virtually no side load or thrust on the bearings since the transverse air loads are balanced. The propeller gearbox, on the other hand, has high radial loads due to its small size and high axial loads since the propeller drag load must be reacted by the propeller thrust bearing. The WWT drag load is equal to the propeller drag load for similar power output but is reacted only by the pivot bearing, which is not in a critical airflow region and can be sized to achieve an optimum cost/benefit ratio.

A careful performance analysis is required relative to coupling the device with the electrical power generator or the mechanical subsystems. This analysis will establish the size, weight, necessary speed controls, mounting height, and other design parameters from which a detailed cost and performance comparison with a competitive-size conventional wind energy system can be carried out.

3.6 Performance Comparison

An idea of the performance of the WWT relative to other types of wind energy conversion devices can be obtained by comparing their performance on the basis of power coefficient, C_p, as is done in Figures 19 and 23. The device most like the WWT, the impulse turbine, has a peak ideal C_p of 1 at a tip speed ratio of 0.5. In practice, the impulse turbine can only realize about 85 to 90 percent of this ideal

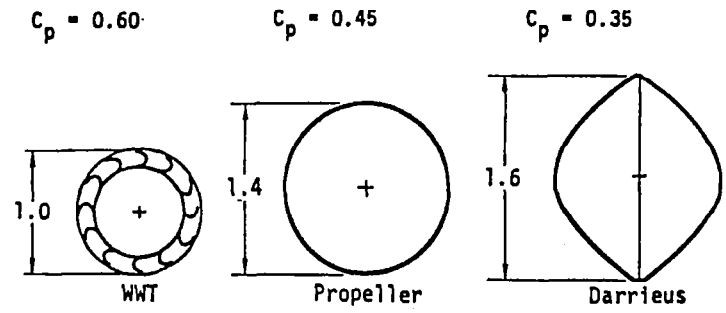

Figure 23 A comparison of the size of the rotating parts of several wind energy extraction devices.

performance in order to limit the diameter of the device due to viscous losses, etc. The potential of the WWT experimental blade arrangement, as noted earlier, is also shown in Figure 19. The salient difference between the WWT and impulse turbine is that the WWT has a lower coefficient of performance that is due to relatively rudimentary internal inlet ducting and the poor treatment of the exhaust gas flow. The apparent advantage of having a positive C_p at values of the tip speed ratio between 1 and 1.35 is believed to be due to the inlet air being directed at a point on the turbine wheel that is 0.74 (i.e., 1/1.35), times the full WWT radius. The improvements in the WWT internal airflow discussed in this paper are expected to increase the efficiency of the WWT and produce a C_p curve more characteristic of an impulse turbine.

The relative diameters of a WWT turbine wheel, propeller, and Darrieus rotor, having C_p's of 0.6, 0.45, and 0.35, respectively, will be 1, 1.4, and 1.6 based on the WWT diameters as shown graphically in Figure 23. We may conclude from this that the WWT rotating parts are smaller and perhaps cheaper than for these competitive systems.

Finally, based on the preceding discussions the projected performance of a 5 kw and 20 kw WWT was computed. Figure 24 shows the results of this comparison. The performance of the WWT based on rated wind speeds of 12 mph and 25 mph are seen to be comparable with that of conventional propeller-type wind generators. For the 5 kw machine the projected power curve was integrated over the annual wind speed distribution based on the Weibull distribution:

Power: 5 kw

Conditions:
- V = 5.36 mps (12 mph)
- D = 40 m
- W/D = 0.375
- η_G = 0.95
- C_p = 0.6
- A = 16.26 m^2
- θ = 35°

Power: 20 kw

Conditions:
- V = 11.2 mps (25 mph)
- D = 6 m
- W/D = 0.2
- η_G = 0.95
- C_p = 0.4
- A = 6.7 m^2
- θ = 17°

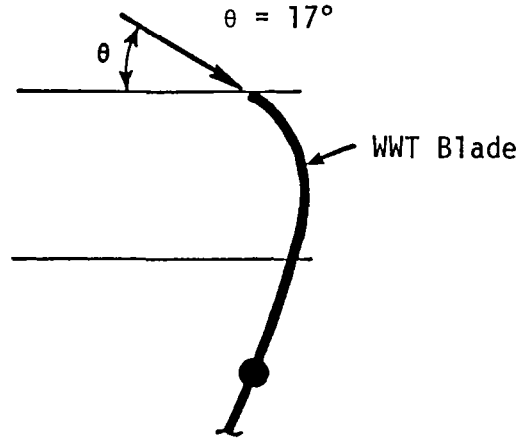

$A = W/D\ \pi D^2 \sin\theta$ = flow capture area

θ = average turbine entry angle

Figure 24 Projected performance.

$$P(V_r \geq V) = \exp[-(V/C_r)k_r]$$

$P(V_r \geq V)$ = probability $V_r \geq V$

where V_r is the steady wind speed at reference elevation (m/s), V is the prescribed value of steady wind speed (m/s), C_r is the Weibull scale factor at reference elevation (m/s), and k_r is the Weibull shape factor at reference elevation. The subscript r indicates the parameter is evaluated at the reference elevation of 10 m. The empirical Weibull constants C_r andk_r will be 5.4 and 2.27 m/s, respectively, defining a siting with a yearly mean wind speed of 5.4 m/s (12 mph) at 9.1 m. The predicted annual output of the wind turbine is 57,816 kw hours.

4.0 CONCLUSIONS

An analysis of the WWT has been carried out. Sufficient information has been provided that specifications for a final design of a functional turbine using off-the-shelf parts and components could be made. This design can now avoid special engineering design and development tasks which are unnecessary and costly; however, final performance of the system can only be determined by field testing a prototype unit.

The conclusion of this study is that the wind-wheel turbine is a viable system offering a number of inherent advantages over a conventional system. Some of these are:

- Wind-wheel turbines with ducted wind concentrators provide C_p's comparable to other conventional wind turbine systems.
- Wind-wheel turbines produce power at low rpm; hence, low vibratory stress, long fatigue life.
- Wind-wheel turbines produce high torque useful for driving pumps and other high-torque mechanical systems.
- Equivalent power output may be achieved with the wind-wheel turbines at lower costs and less risk than competitive systems due to inherently simple construction.

From the results of the study, it is recommended that a prototype system of a roughly 20 to 25 kw power capability be built and field tested.

References

1. Schlichting, H.: Boundary-Layer Theory, 6th edition. New York: McGraw-Hill Book Company, Inc., 1968.

2. Csanady, G. T.: Theory of Turbomachines. New York: McGraw-Hill Book Company, Inc., 1964.

APPENDIX

APPENDIX

PRELIMINARY PERFORMANCE ANALYSIS

The torque and power coefficients for a straight four-bladed wind-wheel are estimated. Consider the wind-wheel with three wind jets V_1, V_2, and V_3 acting upon it as shown in Figure A-1. The forces acting on blades A, B, C, and D will be different in each quadrant but will repeat in subsequent quadrants. Therefore, the forces acting on each blade during a 90° arc need only be calculated. Table A-1 shows typical values of the torque coefficient for the blades individually and as a total. The torque coefficient is defined as

$$C_T = \text{Torque}/\rho V_1^2 wR^2/2 \qquad \text{(A-1)}$$

Calculation of these forces is straightforward but care must be taken to assure that all interaction of the blades and jets are taken into account.

Starting from $\theta = 0$, blade B is acted upon only be jet 1. After a 45° rotation, it is shielded by blade A. During the remaining 45° of travel of blade B, it has a negative force resulting from displacing the air in front of it at a speed of $r\omega$. The expression for C_{T_B} is:

$$C_{T_B} = I_4 + I_5$$

where

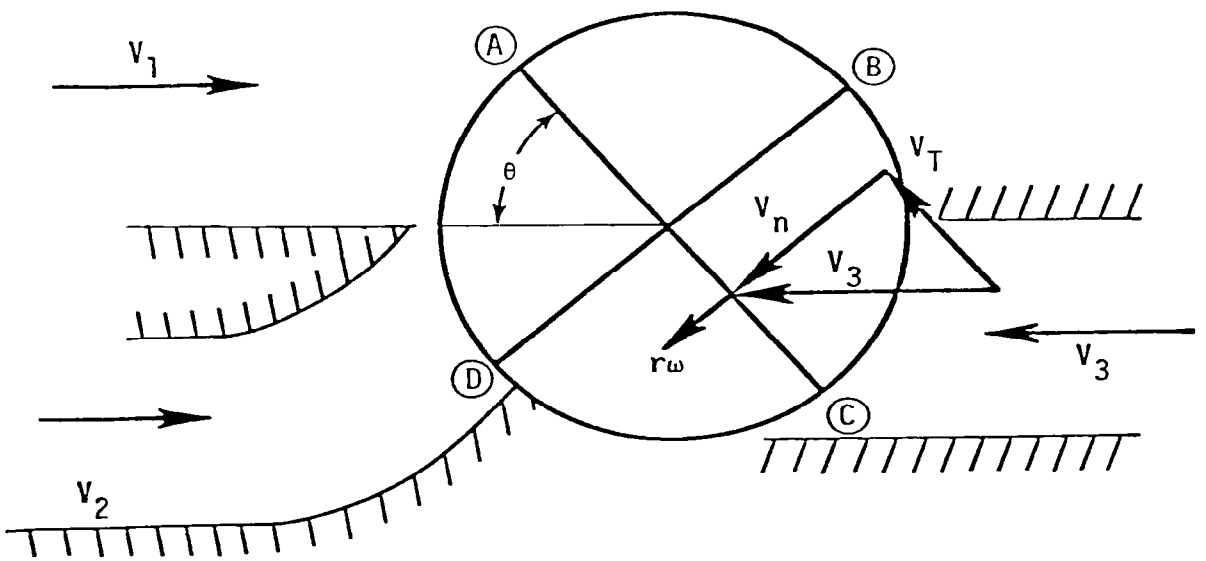

Figure A-1 Definition of jets and blade interaction.

Table A-1 Representative Results of Computed Performance Characteristics.

```
LAMBDA=0.0  XI2=2.0  XI3=0.3
   THETA= 0.   CT=   3.090  CP=   0.000  CPP=   0.000
CTA=0.200E+01  CTB=0.100E+01  CTC=0.000E+00  CTD=0.900E-01
   THETA= 5.   CT=   3.309  CP=   0.000  CPP=   0.000
CTA=0.224E+01  CTB=0.965E+00  CTC=0.664E-03  CTD=0.866E-01
   THETA=10.   CT=   3.481  CP=   0.000  CPP=   0.000
CTA=0.245E+01  CTB=0.940E+00  CTC=0.271E-02  CTD=0.846E-01
   THETA=15.   CT=   3.615  CP=   0.000  CPP=   0.000
CTA=0.266E+01  CTB=0.966E+00  CTC=0.603E-02  CTD=0.779E-01
   THETA=20.   CT=   3.717  CP=   0.000  CPP=   0.000
CTA=0.287E+01  CTB=0.746E+00  CTC=0.105E-01  CTD=0.695E-01
   THETA=25.   CT=   3.795  CP=   0.000  CPP=   0.000
CTA=0.306E+01  CTB=0.643E+00  CTC=0.161E-01  CTD=0.579E-01
   THETA=30.   CT=   3.853  CP=   0.000  CPP=   0.000
CTA=0.325E+01  CTB=0.500E+00  CTC=0.225E-01  CTD=0.450E-01
   THETA=35.   CT=   3.896  CP=   0.000  CPP=   0.000
CTA=0.343E+01  CTB=0.342E+00  CTC=0.295E-01  CTD=0.306E-01
   THETA=40.   CT=   3.930  CP=   0.000  CPP=   0.000
CTA=0.370E+01  CTB=0.174E+00  CTC=0.372E-01  CTD=0.156E-01
   THETA=45.   CT=   3.950  CP=   0.000  CPP=   0.000
CTA=0.391E+01  CTB=0.596E-07  CTC=0.450E-01  CTD=0.536E-06
   THETA=50.   CT=   4.154  CP=   0.000  CPP=   0.000
CTA=0.407E+01  CTB=0.000E+00  CTC=0.528E-01  CTD=0.304E-01
   THETA=55.   CT=   4.295  CP=   0.000  CPP=   0.000
CTA=0.411E+01  CTB=0.000E+00  CTC=0.604E-01  CTD=0.121E+00
   THETA=60.   CT=   4.370  CP=   0.000  CPP=   0.000
CTA=0.403E+01  CTB=0.000E+00  CTC=0.675E-01  CTD=0.206E+00
   THETA=65.   CT=   4.373  CP=   0.000  CPP=   0.000
CTA=0.383E+01  CTB=0.000E+00  CTC=0.739E-01  CTD=0.466E+00
   THETA=70.   CT=   4.295  CP=   0.000  CPP=   0.000
CTA=0.350E+01  CTB=0.000E+00  CTC=0.795E-01  CTD=0.714E+00
   THETA=75.   CT=   4.132  CP=   0.000  CPP=   0.000
CTA=0.305E+01  CTB=0.000E+00  CTC=0.840E-01  CTD=0.100E+01
   THETA=80.   CT=   3.880  CP=   0.000  CPP=   0.000
CTA=0.246E+01  CTB=0.000E+00  CTC=0.873E-01  CTD=0.132E+01
   THETA=85.   CT=   3.533  CP=   0.000  CPP=   0.000
CTA=0.179E+01  CTB=0.000E+00  CTC=0.893E-01  CTD=0.165E+01
   THETA=90.   CT=   3.090  CP=   0.000  CPP=   0.000
CTA=0.100E+01  CTB=0.000E+00  CTC=0.900E-01  CTD=0.200E+01

LAMBDA=0.0  XI2=0.0  XI3=0.1
   THETA= 0.   CT=  -0.066  CP=  -0.054  CPP=  -0.016
CTA=-.160E+00  CTB=0.360E+00  CTC=-.100E+00  CTD=-.110E+00
   THETA= 5.   CT=  -0.033  CP=  -0.020  CPP=  -0.006
CTA=-.118E+00  CTB=0.344E+00  CTC=-.173E+00  CTD=-.110E+00
   THETA=10.   CT=  -0.012  CP=  -0.007  CPP=  -0.002
CTA=-.704E-01  CTB=0.336E+00  CTC=-.166E+00  CTD=-.111E+00
   THETA=15.   CT=  -0.021  CP=  -0.013  CPP=  -0.004
CTA=-.358E-01  CTB=0.286E+00  CTC=-.160E+00  CTD=-.112E+00
   THETA=20.   CT=  -0.053  CP=  -0.032  CPP=  -0.010
CTA=-.107E-01  CTB=0.224E+00  CTC=-.154E+00  CTD=-.113E+00
   THETA=25.   CT=  -0.097  CP=  -0.058  CPP=  -0.018
CTA=0.903E-02  CTB=0.154E+00  CTC=-.146E+00  CTD=-.113E+00
   THETA=30.   CT=  -0.143  CP=  -0.086  CPP=  -0.026
CTA=0.279E-01  CTB=0.805E-01  CTC=-.142E+00  CTD=-.109E+00
   THETA=35.   CT=  -0.179  CP=  -0.108  CPP=  -0.033
CTA=0.501E-01  CTB=0.514E-07  CTC=-.137E+00  CTD=-.971E-01
   THETA=40.   CT=  -0.197  CP=  -0.118  CPP=  -0.036
CTA=0.769E-01  CTB=-.756E-01  CTC=-.133E+00  CTD=-.674E-01
   THETA=45.   CT=  -0.194  CP=  -0.116  CPP=  -0.035
CTA=0.114E+00  CTB=-.180E+00  CTC=-.128E+00  CTD=-.334E-07
   THETA=50.   CT=  -0.331  CP=  -0.198  CPP=  -0.060
CTA=0.154E+00  CTB=-.180E+00  CTC=-.125E+00  CTD=-.160E+00
   THETA=55.   CT=  -0.285  CP=  -0.171  CPP=  -0.052
CTA=0.196E+00  CTB=-.180E+00  CTC=-.121E+00  CTD=-.160E+00
   THETA=60.   CT=  -0.241  CP=  -0.145  CPP=  -0.044
CTA=0.237E+00  CTB=-.180E+00  CTC=-.118E+00  CTD=-.160E+00
   THETA=65.   CT=  -0.199  CP=  -0.120  CPP=  -0.036
CTA=0.276E+00  CTB=-.180E+00  CTC=-.116E+00  CTD=-.180E+00
   THETA=70.   CT=  -0.162  CP=  -0.097  CPP=  -0.030
CTA=0.311E+00  CTB=-.180E+00  CTC=-.114E+00  CTD=-.180E+00
   THETA=75.   CT=  -0.132  CP=  -0.079  CPP=  -0.024
CTA=0.340E+00  CTB=-.180E+00  CTC=-.112E+00  CTD=-.180E+00
   THETA=80.   CT=  -0.109  CP=  -0.065  CPP=  -0.020
CTA=0.362E+00  CTB=-.180E+00  CTC=-.111E+00  CTD=-.180E+00
   THETA=85.   CT=  -0.095  CP=  -0.057  CPP=  -0.017
CTA=0.375E+00  CTB=-.180E+00  CTC=-.110E+00  CTD=-.180E+00
   THETA=90.   CT=  -0.090  CP=  -0.054  CPP=  -0.016
CTA=0.380E+00  CTB=-.180E+00  CTC=-.110E+00  CTD=-.180E+00
```

$$\left.\begin{aligned} I_4 &= 2\int_{\tan\theta}^{1} |\cos\theta - \lambda\tilde{r}|(\cos\theta - \lambda\tilde{r})\tilde{r}d\tilde{r} \\ I_5 &= -2\int_{0}^{\tan\theta} \lambda^2\tilde{r}^3 d\tilde{r} = \frac{-\lambda^2\tan^4\theta}{2} \end{aligned}\right\} ; \; 0 \leq \theta \leq 45°; \; \tilde{r} = \frac{r}{R}$$

$$\left.\begin{aligned} I_4 &= 0 \\ I_5 &= -2\int_{0}^{1} \lambda^2\tilde{r}^3 d\tilde{r} = -\frac{\lambda^2}{2} \end{aligned}\right\} ; \; 45° \leq \theta \leq 90° \qquad \text{(A-2)}$$

Blade C experiences a force due to jet 3 only. This jet results from turning the air through a 180° by the side ducts and a large portion of the wind velocity will be lost. The velocity of jet 3 is therefore $V_3 = \zeta_3 V_1$, where ζ_3 is a small factor. The equation for blade C is:

$$C_{T_C} = I_6$$

where

$$I_6 = 2\int_{0}^{1} |\zeta_3 \sin\theta - \lambda\tilde{r}|(\zeta_3 \sin\theta - \lambda\tilde{r})\tilde{r}d\tilde{r}; \; 0 \leq \theta \leq 90° \qquad \text{(A-3)}$$

Blade D is initially acted upon by jet 3 exactly as blade B. After 45° of rotation, jet 3 no longer acts on blade B; however, at that point jet 2, the air being ducted in from the front and turned through a 45° angle, begins to interact with blade D. This action continues through the remaining 45° of the blade travel. The expression for C_{T_D} is

$$C_{T_D} = I_7 + I_8$$

where

$$I_7 = 2\int_{\tan\theta}^{1} |\zeta_3 \cos\theta - \lambda\tilde{r}|(\zeta_3 \cos\theta - \lambda\tilde{r})\tilde{r}d\tilde{r}; \; 0 \leq \theta \leq 45° \qquad \text{(A-4)}$$

$$I_7 = 0; \; 45° \leq \theta \leq 90°$$

$$I_8 = 0; \; 0 \leq \theta \leq 45°$$

$$I_8 = 2 \int |\zeta_2 \sin(45° - \theta) - \lambda\tilde{r}|(\zeta_2 \sin(45° - \theta) - \lambda\tilde{r})\tilde{r}d\tilde{r} \; ; \; 45° \leq \theta \leq 90°$$

Blade A has the most complicated interaction being acted upon by jets 1 and 2 simultaneously. It is assumed in this simple analysis that the wind speed from jet 1 and that from jet 2 can be superimposed over the portion of the blade upon which they impinge. The velocity of jet 2 is anticipated to be higher than that of jet 1 due to the fact that it has passed through a venturi and accelerated. Thus, $V_2 = \zeta_2 V_1$ where $\zeta_2 \geq 1$. The expression for C_{T_A} is given by:

$$C_{T_A} = I_1 + I_2 + I_3$$

where

$$I_1 = 0; \; 0 \leq \theta \leq 45°$$

$$I_1 = 2 \int_0^{\tan|45° - \theta|} |\sin\theta - \lambda\tilde{r}|(\sin\theta - \lambda\tilde{r})\tilde{r}d\tilde{r}; \; 45° \leq \theta \leq 90°$$

$$I_2 = 2 \int_{LB}^{\cos 45°/\cos|45° - \theta|} |\sin\theta + \zeta_2 \cos|45° - \theta| - \lambda\tilde{r}|(\sin\theta + \zeta_2 \cos|45° - \theta| - \lambda\tilde{r})\tilde{r}d\tilde{r} \qquad \text{(A-5)}$$

where

$$LB = \begin{cases} 0; \; 0 \leq \theta \leq 45° \\ \tan 45° - \theta|; \; 45° \leq \theta \leq 90° \end{cases}$$

$$I_3 = 2 \int_{\cos 45°/\cos|45° - \theta|}^{1} |\sin\theta - \lambda\tilde{r}|(\sin\theta - \lambda\tilde{r})\tilde{r}d\tilde{r}; \; 0 \leq \theta \leq 90°$$

To determine the overall torque coefficient for the four-bladed wheel the torque coefficients for each blade are summed. The torque varies cyclically over a 90° period of rotation.

Power coefficients for the WWT may be computed directly from the torque coefficient as follows:

$$\text{Power} = \omega \cdot \text{Torque}$$

$$C_p = \text{Power}/(\pi V_1^3 wR/2) \qquad \text{(A-6)}$$

substituting Equation 1 gives

$$C_p = \lambda C_T$$

The integral form of Equations A-2 through A-5 were integrated numerically with a Simpson's rule integration scheme for a range of the parameters λ, λ_2, λ_3, and β. Some of these results are plotted in Figures 15 through 18.

1. REPORT NO.	2. GOVERNMENT ACCESSION NO.	3. RECIPIENT'S CATALOG NO.
NASA CR-3532		

4. TITLE AND SUBTITLE	5. REPORT DATE
Theoretical Design Study of the MSFC Wind-Wheel Turbine	March 1982
	6. PERFORMING ORGANIZATION CODE

7. AUTHOR(S)	8. PERFORMING ORGANIZATION REPORT #
Walter Frost and Philip A. Kessel	

9. PERFORMING ORGANIZATION NAME AND ADDRESS	10. WORK UNIT NO.
FWG Associates, Inc. R.R. 2, Box 271-A Tullahoma, Tennessee 37388	M-375
	11. CONTRACT OR GRANT NO. NAS8-34387
	13. TYPE OF REPORT & PERIOD COVERED Contractor Report

12. SPONSORING AGENCY NAME AND ADDRESS	14. SPONSORING AGENCY CODE
National Aeronautics and Space Administration Washington, D.C. 20546	

15. SUPPLEMENTARY NOTES

Marshall Technical Monitor: John W. Kaufman
Final Report

16. ABSTRACT

An analytical and experimental study of an innovative wind-wheel turbine (WWT) is reported. Evaluation of the probable performance, possible practical applications, and economic viability as compared to other conventional wind energy systems is discussed. The WWT apparatus is essentially a bladed wheel which is directly exposed to the wind on the upper half and exposed to wind through multiple ducting on the lower half. The multiple ducts consist of a forward duct (front concentrator) and two side ducts (side concentrators). The forced rotation of the wheel is then converted to power through appropriate subsystems.

Results of a series of preliminary tests on two simple models, a paper model (Model #1) and a stainless steel model (Model #2), are reported. Measured values of power coefficients over wind speeds ranging from 4 to 16 m/s are given. An analytical model of a four-bladed wheel is also developed.

Overall design features of the wind turbine are evaluated and discussed. Turbine sizing is specified for a 5 and 25 kW machine. Suggested improvements to the original design to increase performance and performance predictions for an improved WWT design are given.

17. KEY WORDS	18. DISTRIBUTION STATEMENT
Turbine sizing Performance	Unclassified - Unlimited Subject Category 44

19. SECURITY CLASSIF. (of this report)	20. SECURITY CLASSIF. (of this page)	21. NO. OF PAGES	22. PRICE
Unclassified	Unclassified	42	A03

For sale by National Technical Information Service, Springfield, Virginia 22161

NASA-Langley, 1982